Thermodynamic irreversibility and conjugate effects of integrated microchannel cooling device using TiO$_2$ nanofluid

G. Narendran[1] · N. Gnanasekaran[1] · D. Arumuga Perumal[1]

Abstract

Thermal management is highly essential for the latest electronic devices to effectively dissipate heat in a densely packed environment. Usually, these high power devices are cooled by integrating micro scale cooling systems. Most of the works reported in the literature majorly concentrate on microchannel heat sink in which the characteristics of friction factor and enhancement of heat transfer are analyzed in detail. However, due to the advent of compact electronic devices a crucial investigation is required to facilitate an amicable environment for the neighboring components so as to improve the reliability of the electronic devices. Henceforth, in the present study a combined experimental and numerical analysis is performed to provide an insight to determine the performance of a copper microchannel integrated with aluminium block using TiO$_2$ nanofluid for different particle configurations. Needless to say, the present study, which also focuses on entropy generation usually attributed to the thermodynamic irreversibility, is very much significant to design an optimum operating condition for better reliability and performance of the cooling devices.

Nomenclature

Re	Reynolds number
u	velocity of the fluid (m/s)
k	thermal conductivity (W/m. K)
q''_{bot}	heat flux at the bottom (W/cm^2)
T_∞	room temperature (°C)
n_f	nanofluid
b_f	base fluid
C_p	specific heat (J/kg. K)
n	shape factor
Pr	Prandtl number
V_f	volume fraction
W_1	width of the channel wall
W_2	width of the channel
H	height of the channel
D	diameter of the heater
L	length of the channel
T_w	total width of the channel
P_{in}	pressure at microchannel inlet
P_{out}	pressure at microchannel outlet
T_{in}	temperature inlet
T_{out}	temperature outlet
T_e	temperature of the heater
T_{Al}	temperature of the aluminium block
T_C	temperature of the copper microchannel
$\dot{m}$	mass flow rate
Nu	Nusselt number
$\dot{S}$	total entropy generation

Greek symbols

Δp	pressure drop (Pa)
ρ	density (kg/m^3)
υ_m	mean velocity of the fluid
μ	viscosity (cP)
φ	particle concentration factor

Subscripts

s	solid
f	fluid
p	particle
bot	bottom of the heat sink
m	mean

✉ N. Gnanasekaran
gnanasekaran@nitk.edu.in

1 Department of Mechanical Engineering, National Institute of Technology Karnataka, Surathkal, Mangalore 575025, India

1 Introduction

The recent advances in high end scaling of electronic components have developed more densely packed systems with ultra-speed computational performance. Under operating conditions, these microelectronic chips generate high heat flux,

which demands robust cooling solutions for thermal management in several electronic appliances [1]. But inadequate heat dissipation delivered by the currently available cooling technologies results in the thermal instability of the system under peak computational loads. Hence, optimum thermal dissipation technique is crucial for several such high power systems. One among the effective way is by using microchannel heat sink for electronic cooling introduced by Tuckerman and Pease [2]. This initiated several researchers to perform investigations on different channel structures and working fluids [3–5]. The use of ultrafine nanoparticles in basefluid developed better heat transfer enhancement in electronic cooling systems compared to the traditional working fluids due to its enhanced thermophysical properties coined by Choi [6]. Multiple investigations involving experimental, numerical and analytical aspects of nanofluid [7–10] and hybrid nanofluid [11, 12] are performed for the application of electronic cooling using microchannels [13]. Apart from the studies associated with the augmentation of heat transfer, considerable work is carried out to focus on the possible heat transfer mechanisms involved in nanofluid [14, 15]. Contrarily, the nanofluid negative effects namely pressure drop [16, 17], friction factor [18] and axial back conduction [19] develop energy loss in microchannel to a great extent. Most importantly, embedded microchannel heat sinks are integrated with highly conductive substrates which undergoes simultaneous conjugate cooling effects of the nanofluid and relatively loses high rate of heat due to parasitic heat loads.

From thermodynamics perspective, the energy lost by the integrated devices is irreversible processes termed as exergy and it is proportional to the entropy gained by the system combined with the surroundings [20, 21]. In the latest cooling devices, optimization studies based on irreversibility generated a phenomenal impact in quantifying and minimizing the entropy generation. It deals with the simultaneous assessment of thermal and frictional characteristics of the heat exchangers and its interaction with the surroundings. Previous studies show numerous investigations in optimizing mechanical design parameters of the microchannel. But the operational effects of microchannel embedded cooling system for the application of the densely packed system are not well established. However, minimization of entropy is essential to determine the suitable operating criteria for the system. Moghaddami et al. [22] pointed out that the effects of irreversibility for both the laminar and the turbulent regime are found to reduce when nanofluid was used as a working fluid and at higher turbulent flow rates the effect is still more predominant due to increased viscous dissipation. It is due to the efficient attainment of thermal equilibrium of the nanofluid with the microchannel substrate; as a result, the local temperature gradients are found to get reduced. This results in reduction in entropy generation due to enhanced heat transfer of nanofluid [23]. Li and Kleinstreuer [24] reported that the use of metallic nanofluid

with lower concentration has excellent cooling effect and leads to minimization of entropy generation at lower flow rates.

The entropy generation studies considering nanofluid for electronic applications with integrated structures are less reported in the literature. Heshmatian and Bahiraei [25] conducted numerical investigations on irreversibility developed in circular microchannels using TiO_2 nanofluid by incorporating particle migration and Brownian diffusion effects. It is observed that the particle migration influences the entropy generation. On comparison, nanofluid develops lower thermal entropy generation with increased heat transfer capacity than the pure fluids [26]. Leong et al. [27] performed entropy generation studies with TiO_2 and Al_2O_3 nanofluid at constant wall temperature under both laminar and turbulent regimes. It was found that the use of TiO_2 nanofluid is more efficient than Al_2O_3 nanofluid. However, reduction in entropy generation is not observed for all the investigated turbulent cases. Similar study by Karami et al. [28] investigates entropy generation of Al_2O_3 in a circular tube under constant heat flux. They concluded that using higher volume fraction nanofluid is not appreciable due to its increased frictional entropy generation. For increased volume fractions of TiO_2 nanofluid, the outlet exergy increases at higher flow rates with reduced thermal entropy generation [29, 30]. In many cases the use of nanofluid increases the total entropy generation and the increase is predominately attributed by frictional irreversibility. Sarkar et al. [31] noticed no considerable difference between total entropy generation for both Al_2O_3 and TiO_2 nanofluid for the volume fraction ranging from 0 to 20%. Some of the other entropy generation minimization techniques like increasing fluid inlet temperature and reduction in aspect ratio of the channel are also performed [32].

In microchannel flows, the effect of axial conduction is neglected commonly for the pure fluid cases but the axial conduction effects in microchannel are noticed by using nanofluid. The increased viscosity and thermal conductivity of nanofluid makes the axial conduction effects inevitable in microchannels. Even for fluids with lower Peclet numbers result in increased temperature upstream regions in the channels due to increased axial conduction and form more uniform upstream temperature for higher thermal conductive heat sinks [33]. The theoretical and numerical investigations reported in the literature have neglected the effects of axial conduction which lead extraneous prediction of local heat transfer coefficients. In some of the reported cases of simultaneously developing fluids, the axial conduction showed reduced local Nusselt number at entrance region with considerable deviation in local Nusselt number at outlet region of microchannel [34, 35]. It is pertinent to mention that the proposed correlations in the literature are applicable for the ideal conditions and are difficult to replicate in practical situation without the effects of axial conduction. Moreover, at micro scale level, the axial

conduction has strong effect of inducing different heat patterns at reduced flow rates and develops higher temperatures at microchannel entrance region [36, 37]. Similar results are reported by adding nanoparticles and presented in terms of conduction number in many numerical studies. It is noticed that introduction of nanoparticle increases the critical Reynolds number and develops maximum axial conduction in the cases of higher thermal conductive heat sinks and by using metallic nanofluid [38, 39].

Most of the work reported in the aforementioned literature is about the enhancement of heat transfer and associated irreversibility due to the use of nanofluid in microchannel. At the same time, the practical outcomes of integrating micro heat sinks in densely packed embedded systems have not been adequately dealt with until now. Also, it is quite challenging to analyse the conjugate effects of axial conduction in the microchannel in an integrated system. In general, the effects of axial heat conduction in a channel wall for a standalone microchannel are almost different from the case of densely integrated cooling system. Here, the systems are closely integrated such that the neighboring component experiences thermal load. Moreover, upon packaging heat sinks are integrated to the materials which are not homogenous in all cases, it has several layered structures with different thermal conductivity materials packed as a single module. This allows us to study the additional aspect of understanding the influence of conjugate nature of microchannel in an integrated domain. Besides, from the repeated investigations nanofluid has emerged as a potential working fluid for microscale cooling systems with better heat transfer characteristics. In such cases, it is equally important to look into the conduction effects of the heat sink in both microchannel and its integrated system [33]. The first of these, Hang et al. [37] used very low Reynolds number and experimentally reported the axial conduction effects in microchannel, but the microchannel system is constructed in Polydimethylsiloxane (PDMS) polymer which cannot be used in practical heat transfer application. Suppose, if the same operating condition is imposed in real time situation with integrated system the effect of nanofluid on axial conduction under lower Reynolds number may develop reliability issues in densely packed components, so it is essential to determine the operating conditions of microscale devices in an integrated setup. Ramiar et al. [38] reported a considerable change in axial conduction for the channels of higher aspect ratio in the case of nanofluid. Additional investigations on higher aspect ratio channels support parallel investigations for multi layered microchannels and staged core processers. This combined responses involving non-homogeneity in heat sink, lower Reynolds number and nanofluid coupled with transient time and temperature field has to be established experimentally. To qualitatively replicate the actual situation, the present study proposes integrated heat sink with two different materials. For which copper microchannel is completely integrated in

aluminium block and made as a complete heat sink. Both copper and aluminium metals are chosen due to its high thermal conductivity and their excellent machining capabilities to develop better surfaces with less contact resistance for an integrate heat sink. In this process, apart from the experimentally measured temperature distributions, the temperature dependencies upon entrance and interface are extremely difficult and cumbersome to measure. Hence, numerical analysis is used to support the data for the present investigation. To proceed further, the repeated experimentations are compared with numerical results. The second point is that although several previous work established importance of irreversibility and heat transfer issues involving nanofluid in microchannel, necessary practicality issues are not addressed, e.g., the influence of entropy generation under non-homogenous heatsink, transient temperature distribution in integrated heat sink using nanofluid and the temperature responses due to normal and pulsating pumping.

In the current investigation, all these issues are addressed. A numerical model with integrated domain is presented and used to investigate the heat transfer and irreversibility in a microchannel heat sink for low Reynolds numbers. The numerical model is based on a simplified three-dimensional conjugate heat transfer approach using single phase approach. As a result, the current study focuses on the detailed study of irreversible effects in an integrated microchannel. Both experimental and numerical investigations are carried out using TiO_2 nanofluid in a rectangular microchannel. Particularly, TiO_2 is chosen due to highly established thermo physical model both by means of experimental and numerical. Moreover, TiO_2 nanofluid has higher stability compared to other oxide based nanofluid.

2 Methodology

2.1 Experimental setup

Figure 1 depicts the exploded view of the integrated microchannel heatsink module. It mainly consists of two parts: copper microchannel and aluminium block section. The copper channel is shrink fitted in to the aluminium block and the provision for the fluid to flow is machined in the aluminium block. The complete flow path in the aluminium block is insulated with Teflon to avoid the fluid getting preheated before entering the copper channel. The microchannel is covered with transparent acrylic sheet of 8 mm thickness. The rectangular microchannel was fabricated with nine channels by wire cut electrode discharge machining process. The length of the channel is 36 mm with the channel height of 9 mm, shown in Fig. 2a. Calibrated sheathed thermocouples were used to measure the temperatures of both microchannels and aluminium block which are shown in
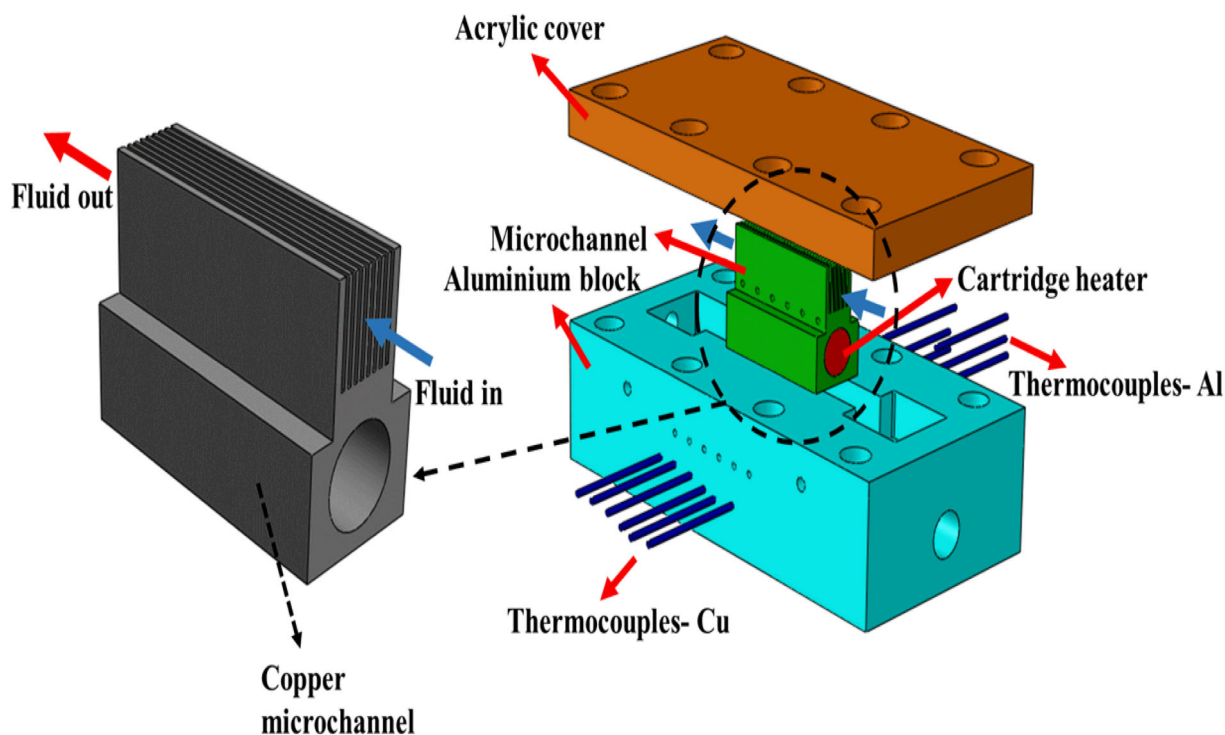
Fig. 1 Model diagram of microchannel experimental setup

Fig. 2b. The side walls of the microchannel and inner wall of the aluminium are milled with minimum surface roughness to reduce the contact resistance. The Scanning electron microscopy (SEM) image of the copper surface is shown in Fig. 2c. However, the surface of the microchannel subjected to Electro discharge machining (EDM) develops surface roughness. The machined surface is measured with surface profile meter that showed a surface roughness of 1.8 μm. Figure 2d, e depicts the SEM image of microchannel side walls. A gasket groove, milled with 6 mm length and 2 mm depth, is maintained throughout the flow path to provide rigid bolting between the acrylic glass cover and the aluminium block. The copper channel is fitted with cartridge heater of 8 mm diameter and 36 mm length to deliver a maximum temperature of 150 °C using flux controller. The pressure drop is measured using pressure transducer (MSE-5200, USA) placed near the inlet and outlet of the channel. 1 mm diameter holes are drilled to insert thermocouples in microchannel. The photograph of the complete integrated module assembly is shown in Fig. 2f.

2.2 Experimental flow line and procedure

The schematic diagram of the experimental flow line is shown in Fig. 3. The fully stabilized nanofluid is passed through the flow line by a peristaltic pump. The fluid flows subsequently to the microchannel channel inlet section; the outlet fluid is circulated in the heat exchanger for temperature regulation and returns to sump. The temperature of the integrated microchannel module is controlled by the cartridge heater

using varying flux controller. The temperature variations in both copper and aluminium are acquired by NI data acquisition module and monitored by a standalone system. The current investigation employs deionized water and TiO_2 nanofluid as working fluids. The nanofluid filled in the sump is subjected to continuous stabilization using magnetic stirrer at very low rpm. The flux controller is operated gradually to increase the temperature of microchannel by varying the voltage supply. The microchannel is allowed to reach a preset temperature of 60 °C above which peristaltic pump is operated. The data from the thermocouples are recorded at higher rates of 70 Hz to measure the instantaneous temperature distribution along the flow. The pressure and temperatures are recorded at inlet and outlet of the microchannel. After 120 s of run time, a difference in temperature of 4 °C was found between inlet and outlet. This procedure is followed for all other working fluids and power ratings. Figure 4 shows the details of the temperature measurement in microchannel.

3 Synthesis of nanofluid and characterization

The nanofluid is synthesized by two stage process and the rutile form of TiO_2 purchased from Merck chemical is dispersed in DI water. Stabilization of the nanofluid is performed by altering the PH and probe sonication. The morphology of the TiO_2 is spherical and reported to have an average diameter of 100 nm mentioned by manufacturer. Figure 5a shows the TiO_2 SEM (JEOL) image at magnification of X 25,000.

Fig. 2 Experimental Details. **a** microchannel dimensions, **b** thermocouple locations, **c** SEM image of the super finished copper wall, **d, e** SEM images of channel surface roughness due to EDM, and **f** complete setup
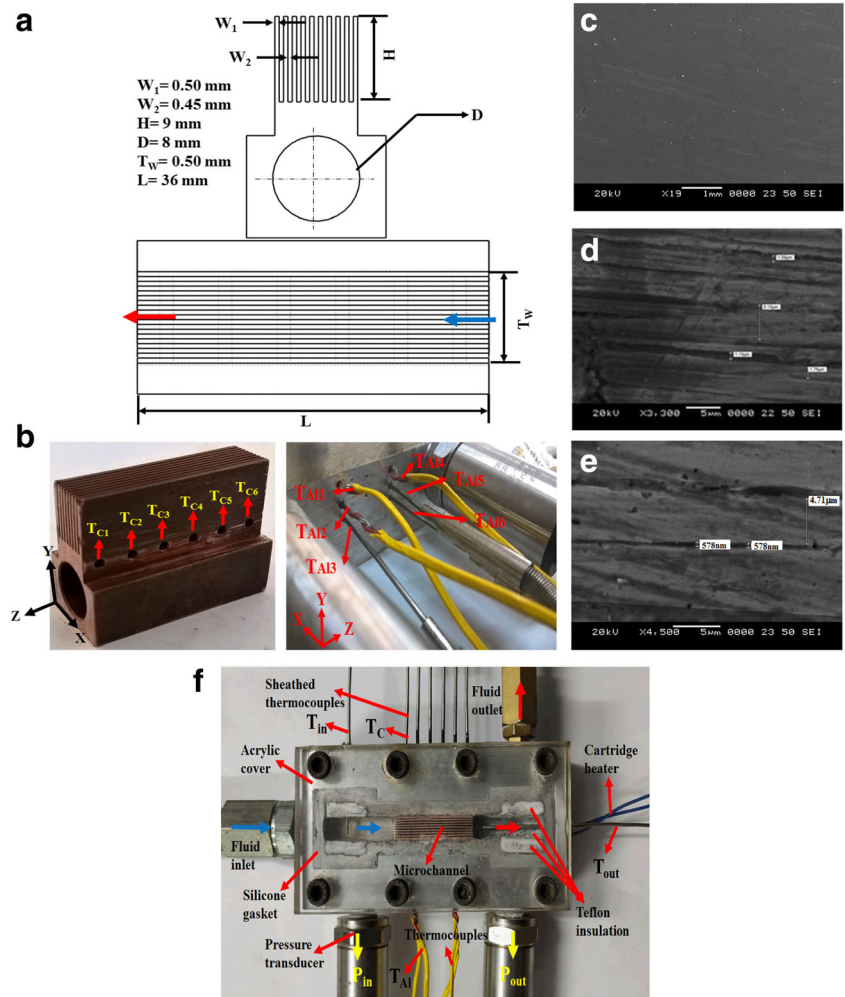
$W_1 = 0.50$ mm
$W_2 = 0.45$ mm
$H = 9$ mm
$D = 8$ mm
$T_W = 0.50$ mm
$L = 36$ mm

Fig. 3 Schematic diagram of the experimental flow line

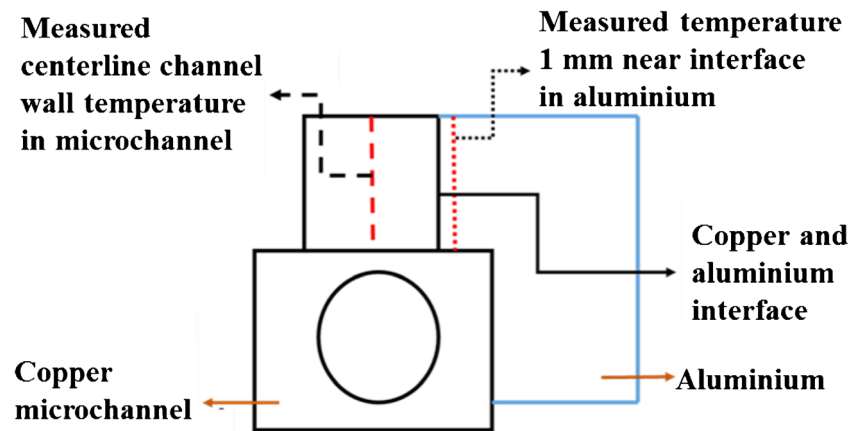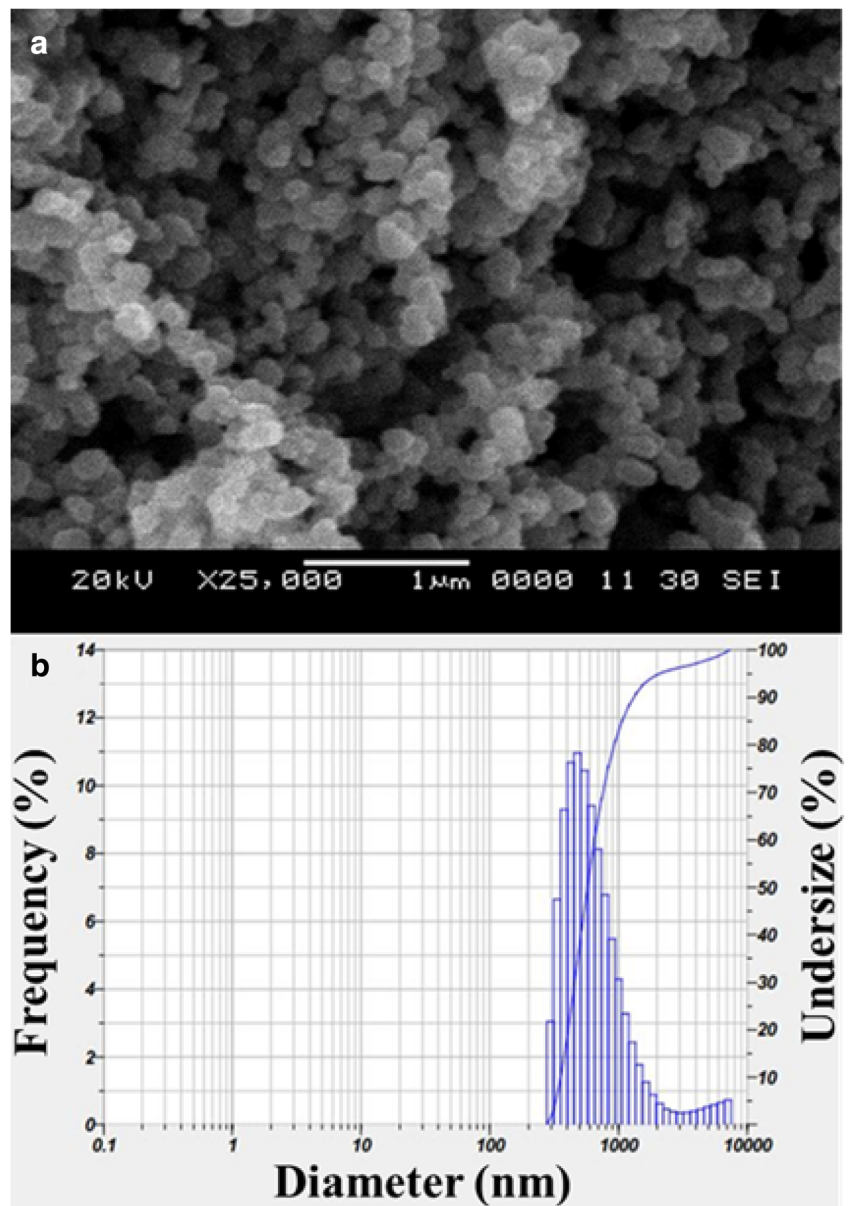**Fig. 4** Details of the temperature
measurement in microchannel

Measured
centerline channel
wall temperature
in microchannel

Measured temperature
1 mm near interface
in aluminium

Copper and
aluminium
interface

Copper
microchannel

Aluminium
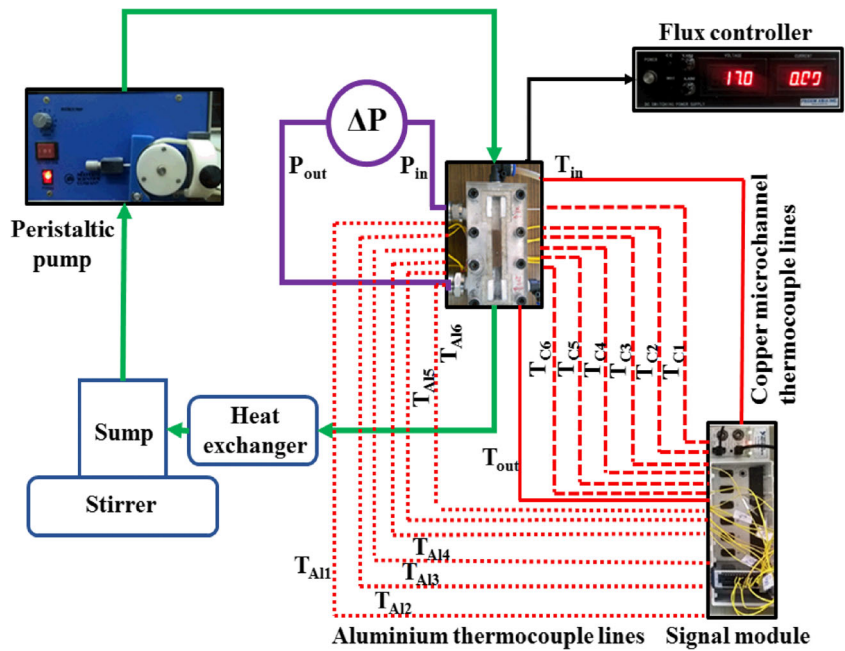
Fig. 5 TiO$_2$ characterization (**a**)
SEM image, **b** particle size
measurement of 0.25% vf using
dynamic light scratting
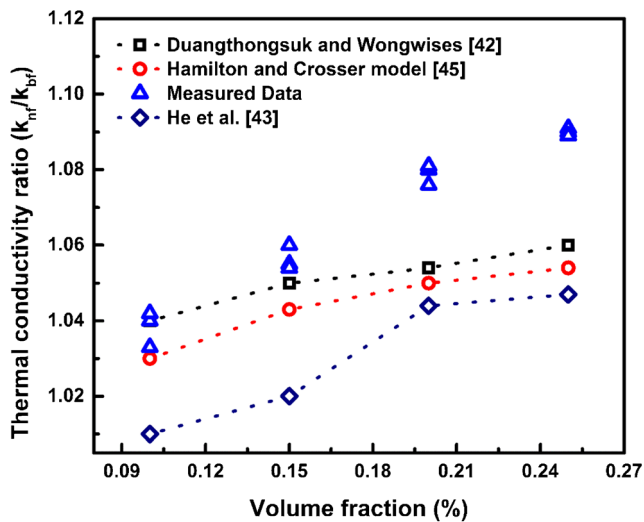
Fig. 6 Effect of particle concentration on effective thermal conductivity of TiO$_2$ nanofluid

Figure 5b shows the average particle size measurement of TiO$_2$ nanofluid using DLS (HORIBA).

3.1 Thermophysical properties of the nanofluid

The experimental study is conducted using the nanofluid consisting of TiO$_2$ nanoparticles with water as the base fluid. The nanofluid is ensured for its homogeneity before proceeding to experiments and finding out its thermophysical properties are of high importance in order to study its heat transfer performance. The nanofluid is subjected to sonication for 40 min to develop highly dispersed mixture with base fluid. The thermal conductivity of the TiO$_2$ nanofluid is measured using thermal conductivity analyser (ABB, Swiss) which provides the values in the form of thermal conductance (1/μΩ).
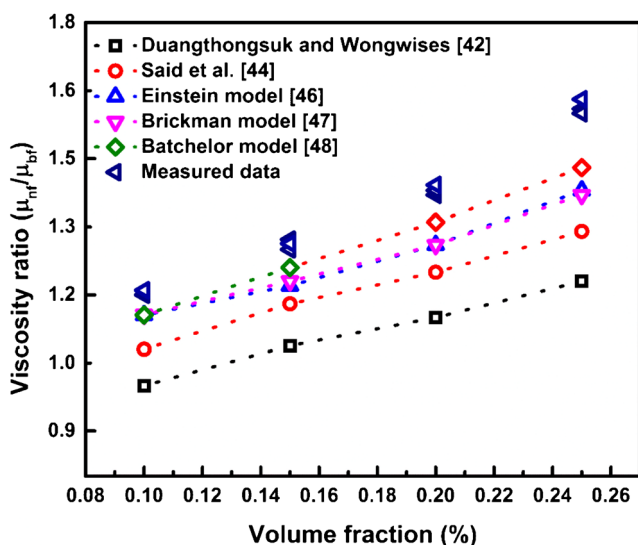

Fig. 7 Effective viscosity of nanofluid on effect of particle concentration

These values are substituted to the correlation to generate the effective thermal conductivity as shown in Fig. 6. The viscosity of the nanofluid is determined using rotary type viscometer presented in Fig. 7. The density and specific heat of the nanofluid (Eqs. 1 and 2) are determined using models of Pak and Cho [40] and Xuan and Roetzel [41], respectively. Additionally, several models on thermal conductivity [42, 43] and viscosity [44] were also compared with the present results.

$$\rho_{nf} = \rho_{bf}(1-\varphi) + \rho_p\varphi \tag{1}$$

$$C_{Pnf} = \frac{\left(\rho_f C_{pf}(1-\varphi) + \rho_p\left(C_{Pp}\varphi\right)\right)}{\rho_f(1-\varphi) + \rho_p\varphi} \tag{2}$$

3.2 Thermal conductivity models

Early studies on determination of the effective thermal conductivity of nanofluid are developed by Maxwell [49] by considering the concept of solid-liquid mixtures. It predicts better results for spherical particles at room temperature for lower particle concentration.

$$\frac{k_{eff}}{k_f} = \frac{k_p + 2k_f + 2\varphi\left(k_f-k_p\right)}{k_p + 2k_f-\varphi\left(k_f-k_p\right)} \tag{3}$$

Hamilton and Crosser [45] introduced shape factor 'n'

$$\frac{k_{eff}}{k_f} = \frac{k_p + (n-1)k_f-(n-1)\left(k_f-k_p\right)\varphi}{k_p + (n-1)k_f + \left(k_f-k_p\right)\varphi} \tag{4}$$

3.3 Viscosity models

The initial classical model on viscosity is developed by Einstein, which considers spherical nanoparticles involving liquid particle interaction in suspension presented as effective viscosity (μ_{eff}). But the model is valid for the nanofluid with particle concentration less than 2%. The Einstein model [46] is given in Eq. 5

$$\mu_{eff} = \mu_f(1 + 2.5\varphi) \tag{5}$$

Extension of the Einstein model is proposed by Brinkman [47] which accounts for lower particle concentration of nanofluid.

$$\mu_{eff} = \mu_f(1 + \varphi)^{-2.5} \tag{6}$$

Einstein model is further modified by including the effects of Brownian motion in nanofluid which is proposed by Batchelor [48] and the model is valid up to 10% of particle concentration.

$$\mu_{eff} = \mu_f \left(1 + 2.5\varphi + 6.2\varphi^2\right) \tag{7}$$

3.4 Data reduction

The present experimental result is validated by comparing with the Shah correlation [50] for Nusselt number which is given in Eq. (8).

$$\mathrm{Nu} = \begin{cases} 1.953 \left(\mathrm{RePr}\dfrac{D_h}{x}\right)^{1/3} \left(\mathrm{RePr}\dfrac{D_h}{x}\right) \geq 33.3 \\ 4.364 + 0.0722 \left(\mathrm{RePr}\dfrac{D_h}{x}\right) \left(\mathrm{RePr}\dfrac{D_h}{x}\right) < 33.3 \end{cases} \tag{8}$$

$$\mathrm{Nu} = \frac{hD_h}{k_{nf}} \tag{9}$$

Where D_h is the hydraulic diameter of the channel and h is heat transfer coefficient and k_{nf} is the thermal conductivity of the nanofluid.

$$D_h = \frac{4W_{ch}H_{ch}}{2(W_{ch} + H_{ch})} \tag{10}$$

Here W_{ch} and H_{ch} are the width and height of the channel.

$$h_l = -\frac{Q_h}{A_c(T_w - T_f)} \tag{11}$$

Where h_l is the local heat transfer coefficient expressed by Eq. (11).

Where A_c is the area of the channel and Q_h is the amount of heat extracted for corresponding wall temperature T_w and inlet fluid temperature T_f. Darcy-Weisbach equation is used to determine the friction factor, expressed by Eq. (12)

$$f = \frac{2D_h \Delta P}{\upsilon_m^2 L \rho} \tag{12}$$

$$P_p = \frac{\dot{m}}{\rho} \Delta P \tag{13}$$

Here, the experimentally measured pressure difference values at the inlet and the outlet of plenum is used to calculate the pumping power as given in Eq. (13). The mean fluid velocity in the microchannel is calculated by using Eq. (14).

$$\upsilon_m = \frac{\dot{m}}{\rho_{nf}(nA_{ch})} \tag{14}$$

Where n is number of channels, $\dot{m}$ is the flow rate in the microchannel.

The outlet exergy of the microchannel heat sink is calculated by using Eq. (15).

$$Ex_{out} = C_{nf} \left(\left(T_{nf,out} - T_e\right) - T_e \ln\left(T_{nf,out}/T_e\right)\right) \tag{15}$$

Where C_{nf} is heat capacity of the nanofluid which can be written as the following Eq. (16)

$$C_{nf} = \left(C_P\right)_{nf} \dot{m} \tag{16}$$

Exergy gain acquired by the cooling fluid is calculated through Eq. (17), where P_p represents the pumping power used in the system given by Eq. (18).

$$Ex_{gain} = (Ex_{out} - Ex_{in}) - P_p \tag{17}$$

$$Ex_{gain} = C_{nf} \left(\left(T_{nf,out} - T_{nf,in}\right) - T_e \ln\left(T_{nf,out}/T_{nf,in}\right) - P_p\right) \tag{18}$$

To determine the total irreversibility developed due to the nanofluid, the sum of entropy generated by heat transfer and fluid friction can be expressed as follows [51].

$$\dot{S} = \dot{S}_{g,HT} + \dot{S}_{g,FF} \tag{19}$$

$$\dot{S}_{g,HT} = \frac{q''^2 \pi D_h^2 L}{kT f_{in} T_{fout} Nu} \tag{20}$$

$$\dot{S}_{g,FF} = \frac{8\dot{m}^3 L}{\pi^2 \rho^2 \left(\dfrac{T_{fin} + T_{fout}}{2}\right)} \cdot \frac{f}{D_h^5} \tag{21}$$

Additionally the total irreversibility contributed by heat transfer and fluid friction can be represented by a non-dimensional number, Bejan number, defined as in Eq. (22) [52].

$$Be = \frac{\dot{S}_{g,HT}}{\dot{S}_{g,HT} + \dot{S}_{g,FF}} \tag{22}$$

4 Numerical methodology

4.1 Governing equations

A single phase model is adopted for the conjugate studies of laminar forced convection heat transfer in a rectangular microchannel. This model involves solving conduction and convection heat transfer simultaneously. The governing equations pertaining to the analysis are given in Eqs. 23–28.

4.1.1 Continuity equation

$$\frac{\partial u}{\partial x} + \frac{\partial u}{\partial y} + \frac{\partial u}{\partial z} = 0 \tag{23}$$

4.1.2 X-momentum equation

$$u\frac{\partial u}{\partial x} + v\frac{\partial u}{\partial y} + w\frac{\partial u}{\partial z} = -\frac{1}{\rho}\frac{\partial p}{\partial x} + v\left(\frac{\partial^2 u}{\partial x^2} + \frac{\partial^2 u}{\partial y^2} + \frac{\partial^2 u}{\partial z^2}\right) \quad (24)$$

4.1.3 Y-momentum equation

$$u\frac{\partial v}{\partial x} + v\frac{\partial v}{\partial y} + w\frac{\partial v}{\partial z} = -\frac{1}{\rho}\frac{\partial p}{\partial y} + v\left(\frac{\partial^2 v}{\partial x^2} + \frac{\partial^2 v}{\partial y^2} + \frac{\partial^2 v}{\partial z^2}\right) \quad (25)$$

4.1.4 Z-momentum equation

$$u\frac{\partial w}{\partial x} + v\frac{\partial w}{\partial y} + w\frac{\partial w}{\partial z} = -\frac{1}{\rho}\frac{\partial p}{\partial z} + v\left(\frac{\partial^2 w}{\partial x^2} + \frac{\partial^2 w}{\partial y^2} + \frac{\partial^2 w}{\partial z^2}\right) \quad (26)$$

4.1.5 Energy equation of the fluid

$$\frac{\partial T}{\partial t} + u\frac{\partial T}{\partial x} + u\frac{\partial T}{\partial y} + u\frac{\partial T}{\partial z} = \alpha\left(\frac{\partial^2 T}{\partial x^2} + \frac{\partial^2 T}{\partial y^2} + \frac{\partial^2 T}{\partial z^2}\right) \quad (27)$$

4.1.6 Energy equation of the solid

$$\frac{\partial^2 T}{\partial x^2} + \frac{\partial^2 T}{\partial x^2} + \frac{\partial^2 T}{\partial x^2} = \frac{1}{\alpha}\frac{\partial T}{\partial t} \quad (28)$$

4.2 Boundary conditions

The fluid is considered as single phase, incompressible laminar without viscous dissipation of energy. The inlet temperature of the fluid is about 28 °C. Laminar fully developed flow and uniform zero pressure is assumed at the outlet, as shown in Fig. 8a. All the walls satisfy the slip condition and both fluid flow and heat transfer are three dimensional.

A laminar forced convection in a rectangular microchannel is considered for the present study by using commercial CFD software FLUENT-14.5. The schematic diagram of the computational model is shown in Fig. 8a. The computational model comprises of two domains namely fluid and solid that corresponds to the copper channel accompanied with aluminium block. The top surface of the channel is covered with acrylic sheet and provided with conduction to convection boundary condition. The interfaces of microchannel and aluminium block are specified with coupled boundary conditions. Single phase approach is used in the present study due to the lower particle concentration of the oxide based nanofluid. The
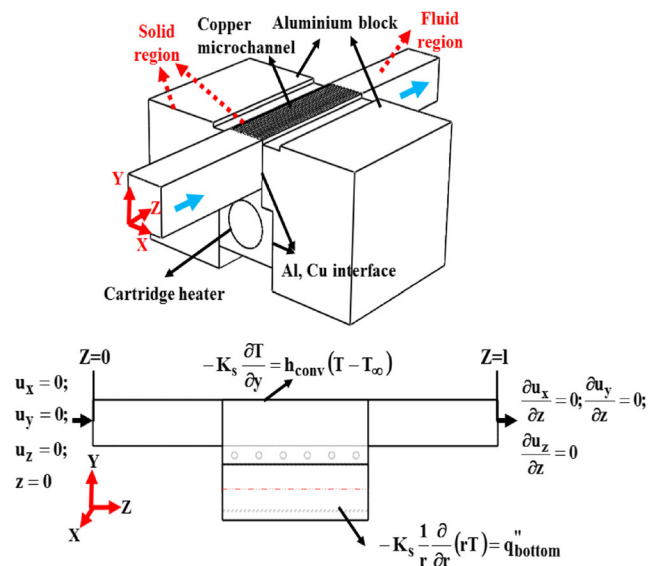

Fig. 8 Schematics of the numerical model. **a** computational domain, and **b** boundary conditions

nanoparticles are considered to be in thermal equilibrium with base fluid. However, several recently published articles have used two-phase models which are far more accurate in the modeling and simulation of nano-convection [53, 54].

4.3 Numerical scheme

The solid and fluid regions are discretized using finite volume method. The entire microchannel is considered for computational domain. Unstructured grid is generated using prismatic elements. Mesh density is increased near the interface region between copper and aluminium by incrementing the mesh density from 2 cells per 0.2 mm^2 to 10 cells shown in Fig. 9. The orthogonal and skewness mesh quality are in the order of 0.79 and 0.14. SIMPLE (Semi-Implicit Method for Pressure Linked Equation) method is chosen to couple pressure and velocity. The convective terms of all governing equations are discretized by a second-order upwind scheme. The resulting algebraic system of equations is solved using Gauss Seidal iterative method with Successive over relaxation (SOR) to improve convergence time. The numerical model is verified with grid independence test and additionally validated with standard experimental results to ensure the fidelity of the computational model and its methodology. The convergence criterion is set to 10^{-6} for all corresponding continuity, momentum and energy terms. Since the model is time dependent, the domain is solved for every time step of 0.0025 s with 100 individual iterations. Every time step the average temperature is obtained and compared with experimental results. The grid system employed in the numerical analysis has 1660824

Fig. 9 Microchannel heat sink with finite volume mesh
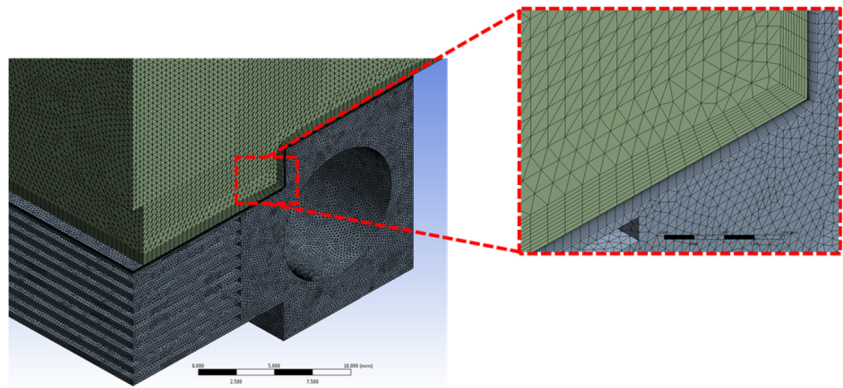
elements. The sensitivity of the numerical results is checked with different grid ranging from 297184 to 3727937 as presented in Fig. 10. There is no considerable change in the results beyond the grid size of 1660824. Hence, the grid size of 1660824 is used for further numerical simulations in order to minimize the computational time.

5 Uncertainty analysis

All the experimental data collected are subjected to errors due to the associated uncertainties which are separately listed in Table 1. The uncertainty associated with the individual irreversibility and heat transfer parameters such as power input to cartridge heater, heat extracted by working fluid, Nusselt number, exergy gain, outlet exergy, second law efficiency and entropy generation quantification is performed using propagation analysis [55].

From the analysis the uncertainty involved in Nusselt number, outlet exergy, second law efficiency and entropy generation are ±4%, ±8%, ±6%, and ± 5% respectively.
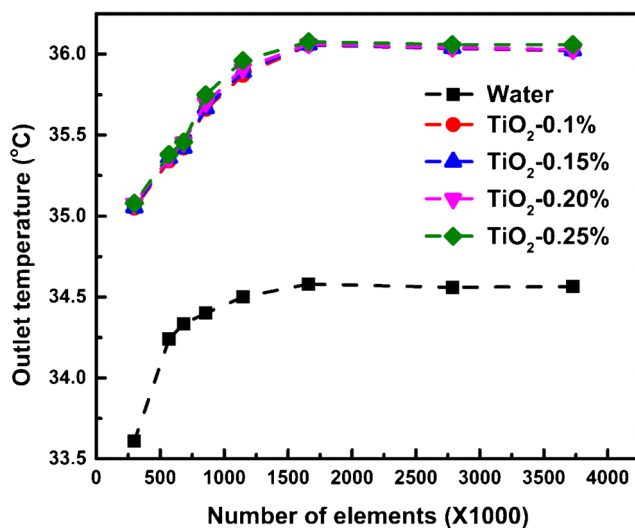

Fig. 10 Grid independence study

6 Results and discussion

6.1 Validation study

Laminar forced convection experiments are conducted under very low flow rate of 200 ml/min using DI-water with a constant heat flux condition. The obtained results provide considerable agreement with the benchmark Shah Equation [50]. Figure 11 shows the comparison of Nusselt number results along the length of the flow. Figure 12 represents the comparison of friction factor with respect to the flow rate. With a maximum deviation of 5%, a good agreement between the experimental and analytical results was found.

6.2 Temperature study

Figure 13 shows the comparison between numerical and experimental studies of temperature along the length of the channel at a fixed flow rate of 200 ml/min. The presented temperature measurements were obtained from six thermocouples (T_{C1} to T_{C6}). An appreciable agreement is obtained with minor deviations due to the use of multiple

Table 1 List of uncertainty parameters

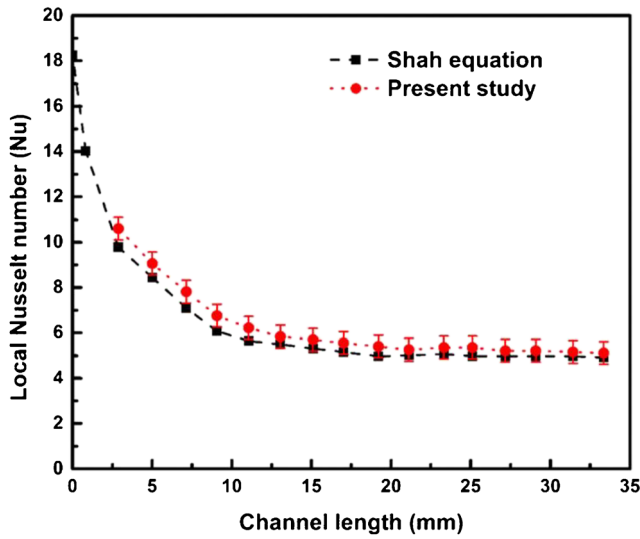| Uncertainty parameters	Uncertainty (%)
Thermal conductivity, (W/mK)	±1.0
Density, (kg/m³)	±1.0
Viscosity, (cP)	±0.12
Specific heat, (J/kg K)	±1.0
Ambient temperature, (°C)	±1.0
Voltage, (V)	±2.0
Current, (A)	±2.0
Mass flow rate,(kg/s)	±2.5
Temperature difference (T_{out}-T_{in}), (°C)	±2.0
Temperature of copper sink, (°C)	±2.0
Temperature of aluminium block, (°C)	±2.0
Pressure Transducer, (kPa)	±3.0

Fig. 11 Nusselt number variation along the channel length

Fig. 13 Comparative study on temperature variation along the length of the channel for a flow rate of 200 ml/min

thermocouples. Transient temperature measurement comparison upon single thermocouple is presented in Fig. 14 with qualitatively better agreement. It shows the decrease in temperature for a flow period of 120 s using pure fluid at a flow rate of 200 ml/min with normal and pulsating flow. Comparatively, slight decrease in temperature was observed for pulsating flow than normal flow in both microchannel and aluminium block section. As soon as the flow starts, a steep decrease and a temperature drop of 12 °C is observed within 3 s in copper channel. The reduction in temperature is observed as the flow progresses and remains nearly 7 °C more than the inlet fluid. But the temperature decrease in the aluminium block is very gradual compared to the copper channel. Since, the materials under investigation possess high thermal conductivity, the temperature difference measured between aluminium and copper channel core is more or less similar
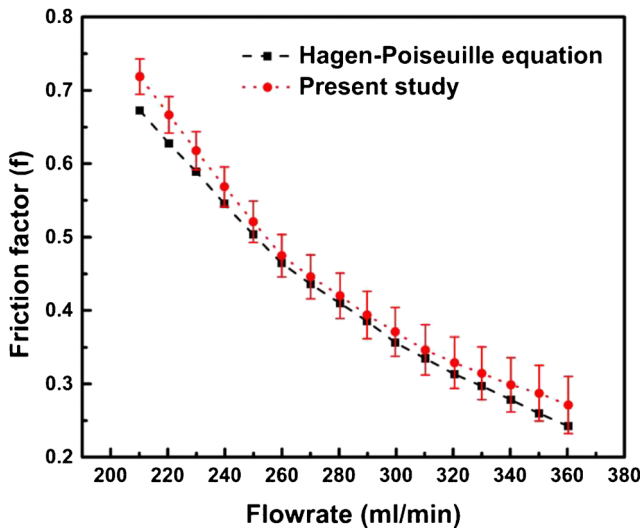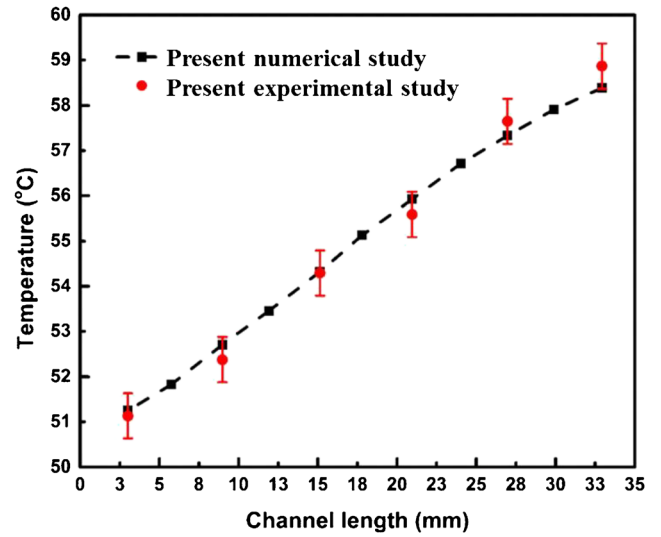
when the flow is initiated. Due to the conjugate effect, the direct cooling of copper channel influences the temperature of aluminium block. Figure 15 depicts the decrease in temperature for different power factors ranging from 14 W to 20 W. For a constant mass flow rate of 200 ml/min, 20 W power consumes more working fluid to attain the room temperature and in other hand 14 W reaches room temperature within 75 s of runtime by using minimal working fluid.

6.3 Exergy analysis

The outlet exergy for different volume fractions of TiO$_2$ for increase in flow rate is calculated and presented in Fig. 16. It is observed that the maximum outlet exergy is developed by using TiO$_2$ nanofluid with 0.25% volume fraction generating outlet exergy of 150 W which is 80% more than

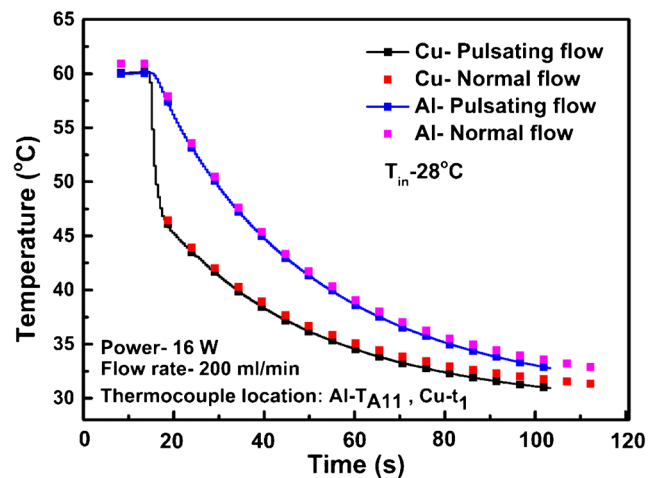Fig. 12 Friction factor comparison for increased flow rate

Fig. 14 Comparative study on transient temperature decrement as function of time
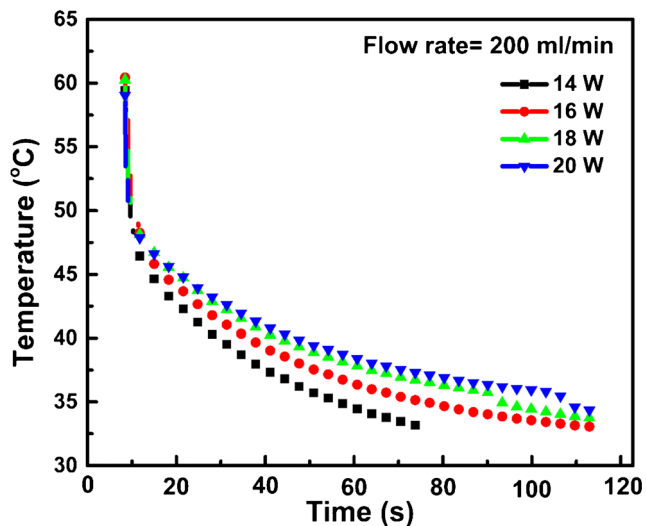
Fig. 15 Temperature reduction in channel for different power with constant flow rate using water

Fig. 17 Exergy gain for different nanofluid concentrations as a function of flow rate

that of water for the same flow rate of 410 ml/min. This increase in outlet exergy is highly contributed to increased thermal conductivity of the working fluid at higher volume fractions. On the other hand, increase in flow decreases the exergy gain which is presented in Fig. 17 and a maximum gain of 112 W is developed for 0.25% of TiO₂ at a lower flow rate of 210 ml/min but with the increase in flow rate the exergy gain reduced considerably. This decrease in exergy gain can be attributed to the increased flow rate. This effect is predominately found between water and TiO₂ nanofluid and the deviation between TiO₂ volume fractions is very minimal. For the same flow rate condition, the pure fluid developed a reduction of exergy gain of 12 W. This trend is contributed to increase in sink temperature for increased flow rate.
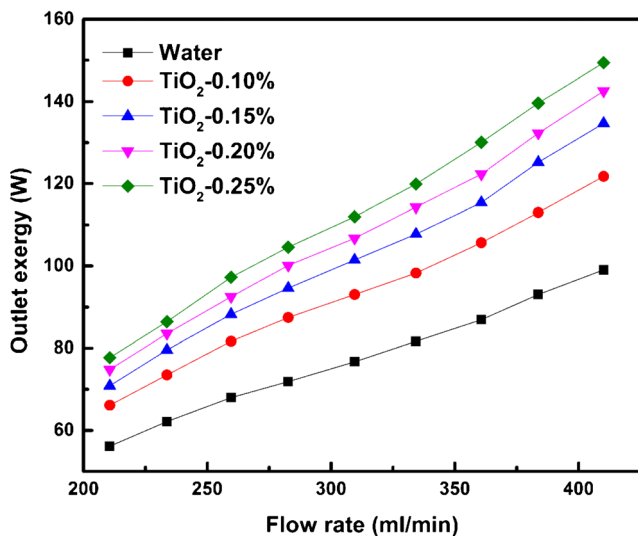
6.4 Entropy generation study

The entropy generated for different TiO₂ nanofluid is discussed in Figs. 18 and 19. Figure 18 depicts the thermal entropy generation and Fig. 19 represents the entropy generated from fluid friction which is calculated from Eqs. 20 and 21. It is observed that increasing thermal conductivity of the fluid combined with increased flow tend to reduce the thermal entropy generation. The thermal entropy generated by TiO₂–0.25% is about 0.044 W/K and 0.02 W/K for flow rates of 210 ml/min and 410 ml/min respectively. In contrast, frictional entropy increases with the increased flow rate and the contribution of the frictional entropy is lower when compared with the thermal entropy generation. It majorly takes into account of increase in friction along the flow length. The maximum frictional entropy is
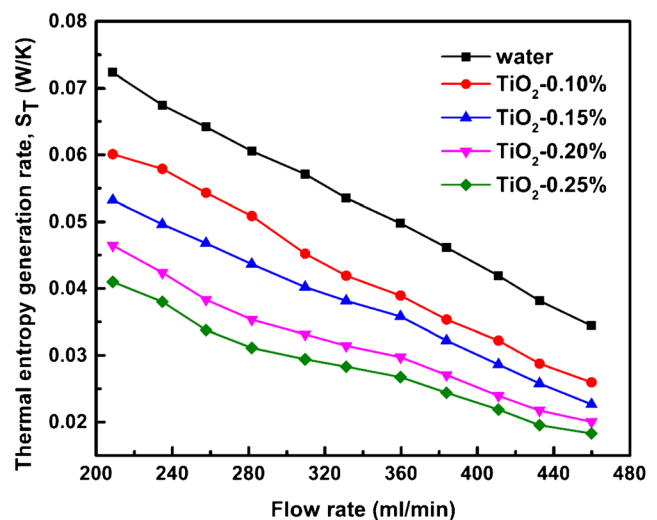

Fig. 16 Outlet Exergy for different nanofluid concentrations as a function of flow rate

Fig. 18 Thermal entropy generation rate for different nanofluid concentrations
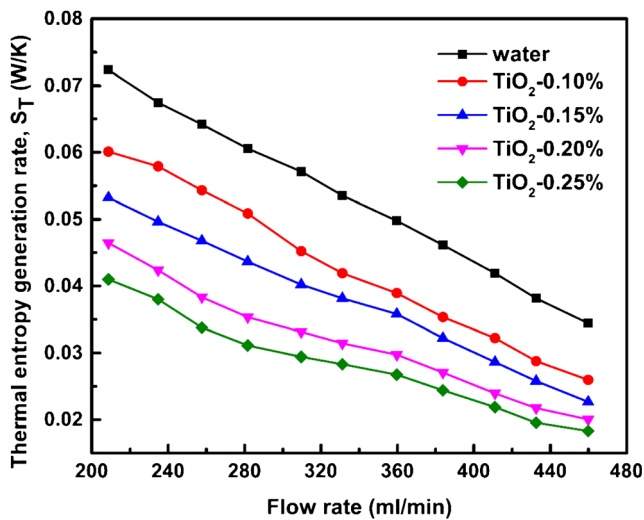
Fig. 19 Frictional entropy generation rate for different nanofluid concentrations

developed for highest mass flow rate of 460 ml/min compared to the increment of TiO$_2$–0.25% which is 6% more than that of TiO$_2$–0.01% and 9% more than pure fluids. Frictional entropy generation is relatively lower than the thermal entropy which is primarily due to the increased aspect ratio of microchannels. Additionally, higher difference in frictional entropy is observed for higher volume fraction of TiO$_2$–0.25% and water at increased flow rate.

Figure 20 presents the Bejan number (Be) as a function of flow rate for different TiO$_2$ nanofluid concentrations. As observed, the effect of thermal entropy generation is higher than frictional entropy generated. Compared to the water, even with the use of very low volume fraction of TiO$_2$–0.25%, increase in frictional entropy generation is found. Additionally, at higher stability the viscosity of oxide based TiO$_2$ nanofluid is higher
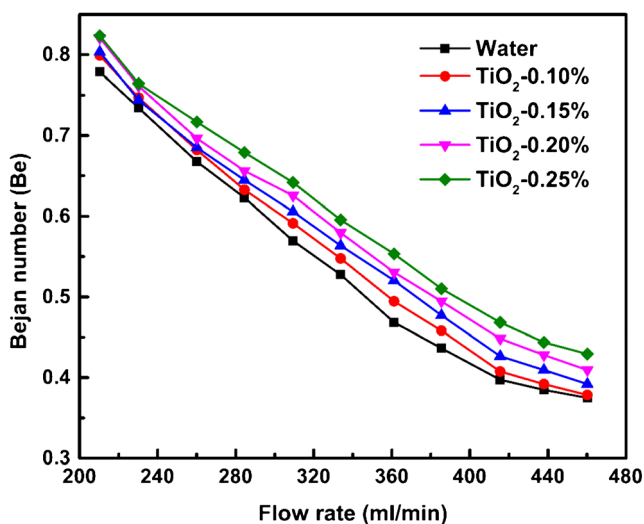

Fig. 20 Bejan number variations as a function of flow rate for different TiO$_2$ nanofluid concentrations

and leads to increased particle to particle and particle to surface interactions. This decreases the Bejan number for higher TiO$_2$ particle concentrations subjected to increased flow rates. The Bejan number is found more or less near the value ranging from 0.40 to 0.85.

Figure 21 presents the effect of TiO$_2$ concentration on forced convection enhancement in the microchannel heat sink. It shows the temperature contours along the length of the flow in microchannel and the surrounding aluminium block. It is clear that the maximum temperature in all the simulated cases is located near the outlet region of the heat sink, and by using nanofluid peak temperature of the heat sink decreases.

Figure 21a shows the temperature distribution of the channel and the aluminium block with water as working fluid for 12 W subjected to the flow rate of 200 ml/min. Maximum decrease in temperature is observed near the entrance region of the microchannel and accordingly the surrounding aluminium block temperature is also reduced. Highest temperature of 55 °C is noticed near the heater. For the same flow rate by using 0.25%-TiO$_2$ nanofluid the maximum temperature is reduced to 53 °C and outlet temperature increased to 38 °C. Due to the increased thermal conductivity of the fluid, the effects of axial thermal conduction of microchannel cooling are extended throughout the aluminium block, shown in Fig. 21b. On other hand the cooling effect in aluminium block is noticed highly parallel to microchannel for increased flow rate of 460 ml/min, shown in Fig. 21c. For the increased flow rate of 460 ml/min the cooling effects near the inlet as observed in the flow rate of 200 ml/min is not noticed due to reduced axial conduction. This reduces the conjugate cooling effects and provides the temperature contour distribution in aluminium block parallel to the channel flow. Similar trend is observed in TiO$_2$–0.25% nanofluid with reduced temperature near the channels as shown in Fig. 21d. Figure 21e, f shows the temperature distribution for the power of 18 W. For the flow rate of 200 ml/min maximum temperature of the sink reached up to 67 °C shown in Fig. 21e. Outlet temperature for TiO$_2$–0.25% increased to 41 °C shown in Fig. 21f. Additionally, the difference in temperature distribution trend for 460 ml/min is more or less identical when compared with 200 ml/min as shown in Fig. 21g, h.

Figure 22 depicts the temperature iso-surfaces at constant flow rate of 460 ml/min for different TiO$_2$ volume fractions. Figure 22a presents temperature iso-surfaces for water as working fluid. It is seen that maximum temperature of 46 °C prevails near the channel floor. Above that second highest fluid temperature layer of 42 °C is observed which is noticed from beginning of the microchannel. The predominant fluid temperature of 36 °C is found above the second layer. Further, temperature iso- surfaces in

Fig. 21 Temperature contours for different volume fractions, flow rates and Power factor
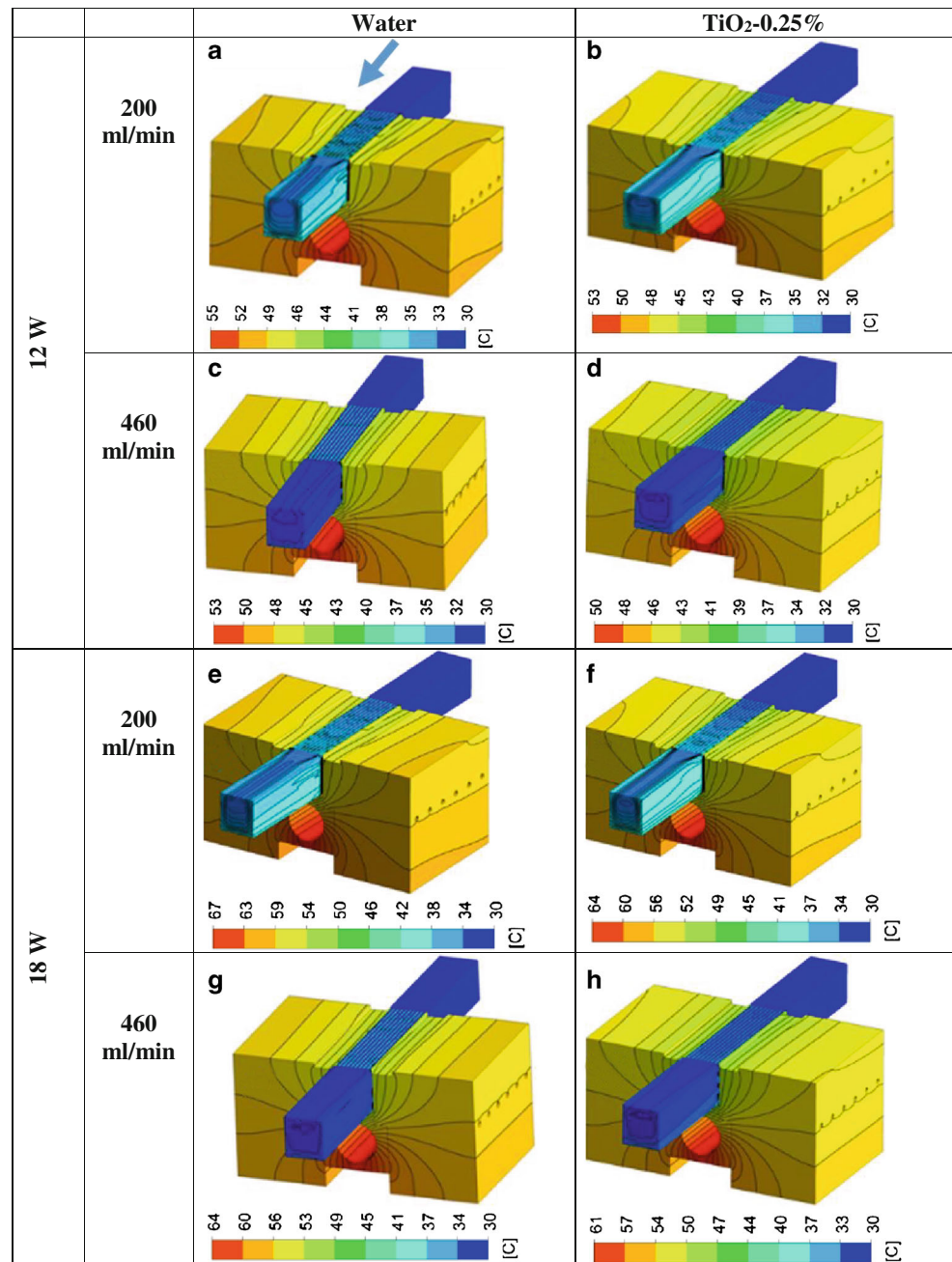
aluminium block near the entrance region found parabolic due to the entrance effect and further along the length of the flow it moves inward to the channel wall. In this case, the effect of cooling is noticed in the aluminium near the vicinity of the microchannel which was not seen in other cases, shown in Fig. 22b–e. Figure 22b depicts the temperature iso-surfaces for TiO$_2$–0.10%, compared with the water the maximum outlet temperature of 46 °C has increased and predominant fluid temperature of 36 °C reduced by 20%. Additionally, last channels of the heatsink develop the maximum outlet temperature which is seen throught out the channel height, shown in Fig. 22c. Due to the increased thermal conductivity of the nanofluid the iso-surface for the 36 °C decreased nearly half when compared with water. Furthermore, for working fluid TiO$_2$–0.20%, 36 °C is reduced drastically and majority of the fluid is present at the top edge of central channels as shown in Fig. 22d. Figure 22e depicts the completely disappeared temperature iso-surface of 36 °C and completely filled 46 °C temperature iso-surface near the outlet of the channel. This is highly attributed to the increased thermal conductivity of the working fluids.

Fig. 22 Temperature iso-surfaces for outlet fluid and aluminium block for different TiO$_2$ nanofluid at a constant flow rate of 460 ml/min with power factor of 18 W. **a** Water, **b** 0.1%, **c** 0.15%, **d** 0.20%, and **e** 0.25%
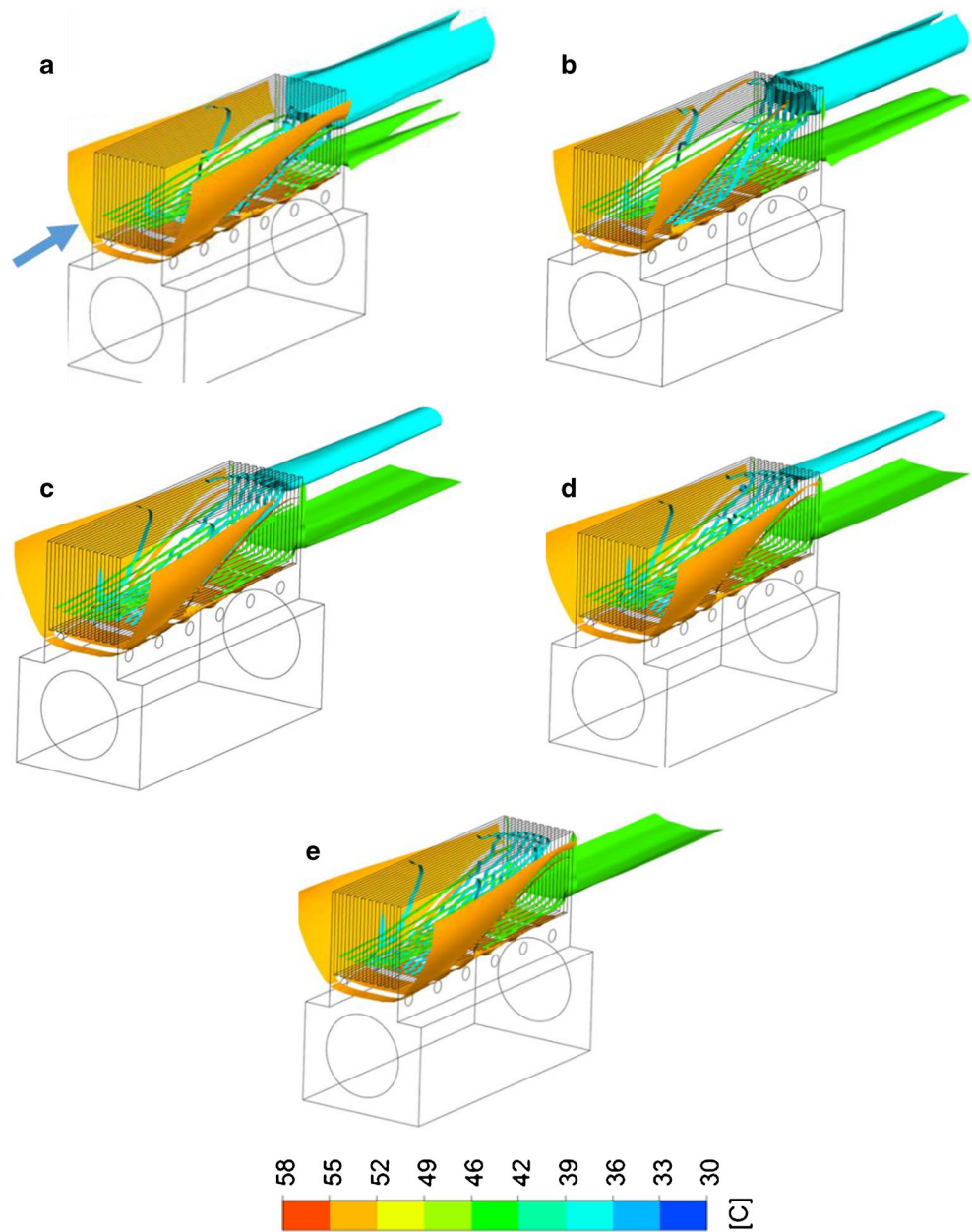
7 Conclusions

In this study, the exergy, entropy generation, fluid hydrodynamics and heat transfer characteristics for a deep rectangular microchannel was investigated using TiO$_2$ nanofluid at different volume fractions. From the combined numerical and experimental studies the following key findings are listed:

- From the experiments, it has been observed during heating, the temperature difference between the copper and aluminium block approaches almost to 4 °C but after sometime a steep decrease in temperature was observed while cooling in case of copper microchannel but the same was not noticed for aluminium block.

- Most importantly the entrance effect was not only observed in microchannel but also in the integrated regions of the microchannel. Also, when the flow rate is increased temperature isotherms were parallel in aluminium block.

- The nanofluid significantly reduces the temperature difference between the microchannel walls and the mean temperature of the fluid in the microchannel. More than the conjugate effects increase in volume fraction reduces the thermal resistance between the microchannel wall and fluid thereby elevating the outlet temperature to a great extent.

- The significant effects of axial thermal conduction at inlet and outlet of microchannels are mainly observed for TiO_2 nanofluid at lower flow rate. This axial conduction extends in aluminium block predominantly near inlet section and reduces for higher flow rates. For the maximum flow rate of 460 ml/min, the axial conduction becomes constant throughout the microchannel and effect of conjugate heat transfer is decreased.
- On analyzing the thermal and fluid hydrodynamics the conjugate effects were witnessed higher for TiO_2 nanofluid than water. The variation in conjugate effects among the TiO_2 nanofluid was found much similar. The increased flow rate influences the conjugate effect for both water and TiO_2 nanofluid.
- It was found that with the increase in flow rate, the outlet exergy increases for all the subjected TiO_2 nanofluid concentrations. The highest outlet exergy of 145 W was observed for the flow rate of 410 ml/min.
- Thermal entropy generation decreases for higher TiO_2 nanofluid concentration and flow rate. The frictional entropy generation increases for higher flow rate and nanofluid particle concentration.

References

1. Moore GE (1998) Cramming more components onto integrated circuits. Proc IEEE 86(1):82–85
2. Tuckerman DB, Pease RF (1981) High-performance heat sinking for VLSI. IEEE Electronic Devices Lett 2(5):126–129
3. Zhang LY, Zhang YF, Chen JQ, Bai SL (2015) Fluid flow and heat transfer characteristics of liquid cooling microchannels in LTCC multilayered packaging substrate. Int J Heat Mass Transf 84:339–345
4. Moradi HV, Floryan JM (2013) Maximization of heat transfer across micro-channels. Int J Heat Mass Transf 66:517–530
5. Parlak Z (2018) Optimal design of wavy microchannel and comparison of heat transfer characteristics with zigzag and straight geometries. Heat Mass Transf 54(11):3317–3328
6. Choi SUS (1995) Enhancing thermal conductivity of fluids with nanoparticle. ASME Fluids Eng Div 231:99–105
7. Bhattacharya P, Samantha AN, Chakraborty S (2009) Numerical study of conjugate heat transfer in rectangular microchannel heat sink with Al_2O_3/H_2O nanofluid. Heat Mass Transf 45(10):1323–1333
8. Rimbault B, Nguyen CT, Galanis N (2014) Experimental investigation of CuO-water nanofluid flow and heat transfer inside a microchannel heat sink. Int J Thermal Sci 84:275–292
9. Anoop K, Sadr R, Yu J, Kang S, Jeon S, Banerjee D (2012) Experimental study of forced convective heat transfer of nanofluids in a microchannel. Int Commun Heat Mass Transf 39(9):1325–1330
10. Ahmed M, Eslamian M (2015a) Laminar forced convection of a nanofluid in a microchannel: effect of flow inertia and external forces on heat transfer and fluid flow characteristics. App Thermal Eng 78:326–338
11. Nimmagadda R, Venkatasubbaiah K (2015) Conjugate heat transfer analysis of micro-channel using novel hybrid nanofluids (Al_2O_3+ ag/water). Eur J Mech B Fluids 52:19–27
12. Narendran G, Gnanasekaran N, Perumal DA (2018b) A review on recent advances in microchannel heat sink configurations. Patent Mech Eng 11(3):190–215
13. Brinda R, Daniel RJ, Sumangala K (2012) Ladder shape micro channels employed high performance micro cooling system for ULSI. Int J Heat Mass Transf 55(13–14):3400–3411
14. Eslamian M, Saghir MZ (2014) On thermophoresis modeling in inert nanofluids. Int J Thermal Sci 80:58–64
15. Ahmed M, Eslamian M (2015b) Numerical simulation of natural convection of a Nanofluid in an inclined heated enclosure using two-phase lattice Boltzmann method: accurate effects of thermophoresis and Brownian forces. Nanoscale Res Lett 10:296
16. Dominic A, Sarangan J, Suresh S, Devahdhanush VS (2017) An experimental study of heat transfer and pressure drop characteristics of divergent wavy minichannels using nanofluids. Heat Mass Transf 53(3):959–971
17. Arshad W, Ali HM (2017) Experimental investigation of heat transfer and pressure drop in a straight minichannel heat sink using TiO_2 nanofluid. Int J Heat Mass Transf 110:248–256
18. Yin Z, Bao F, Tu C, Hua Y, Tian R (2018) Numerical and experimental studies of heat and flow characteristics in a laminar pipe flow of nanofluid. J Exp Nanosci 13:82–94
19. Moharana MK, Khandekar S (2012) Effect of aspect ratio of rectangular microchannels on axial back conduction in its solid substrate. Int J Microscale Nanoscale Thermal Fluid Trans Phenomena 4(3–4):211–229
20. Bejan A (1996) Entropy generation minimization. CRC press, Roca Raton
21. McHale JP, Garimella SV (2010) Heat transfer in trapezoidal microchannels of various aspect ratios. Int J Heat Mass Transf 53:365–375
22. Moghaddami M, Mohammadzade A, Esfehani SAV (2011) Second law analysis of nanofluid flow. Energy Convers Manag 52(2):1397–1405
23. Mahian O, Kianifar A, Kleinstreuer C, Al-Nimr MA, Pop I, Sahin AZ, Wongwises S (2013) A review of entropy generation in nanofluid flow. Int J Heat Mass Transf 65:514–532
24. Li J, Kleinstreuer C (2010) Entropy generation analysis for nanofluid flow in microchannels. J Heat Transf 132(12):122401, 1–122401, 8
25. Heshmation S, Bahiraei M (2017) Numerical investigation of entropy generation to predict irreversibilities in nanofluid flow within a microchannel: effects of Brownian diffusion, shear rate and viscosity gradient. Chem Eng Sci 172:52–65
26. Sohel MR, Saidur R, Hassan NH, Elias MM, Khaleduzzaman SS, Mahbubul IM (2013) Analysis of entropy generation using nanofluid flow through the circular microchannel and minichannel heat sink. Int Commun Heat Mass Transf 46:85–91
27. Leong KY, Saidur R, mahilia TMI, Yaru YH (2012) Entropy generation analysis of nanofluid flow in a circular tube subjected to constant wall temperature. Int Commun Heat Mass Transf 39(8):1169–1175
28. Karami M, Shirani E, Avara A (2012) Analysis of entropy generation, pumping power, and tube wall temperature in aqueous suspensions of alumina particles. Heat Transf Res 43(4):327–342
29. Narendran G, Bhat MM, Akshay D, Perumal DA (2018a) Experimental analysis on exergy studies of flow through a minichannel using TiO_2/water nanofluid. Thermal Sci Eng Prog 8:93–104
30. Chamka AJ, Molana M, Rahnama A, Ghadami F (2018) On the nanofluids applications in microchannels: a comprehensive review. Powder Technol 322:287–322

31. Shankar S, Ganguly S, Dalal A (2012) Analysis of entropy generation during mixed convection heat transfer of nanofluids past a square cylinders in vertically upward flow. J Heat Transf 134(12):122501, 1–122501, 8

32. Manay E, Akyurek EF, Sahin B (2018) Entropy generation of nanofluid flow in a microchannel heat sink. Results Phys 9:615–624

33. Yu F, Wang T, Zhang C (2018) Effect of axial conduction on heat transfer in a rectangular microchannel with local heat flux. J Thermal Sci and Technol 13(1):1–13

34. Moharana MK, Agarwal G, Khandekar S (2011) Axial conduction in single phase simultaneously developing flow in a rectangular mini-channel array. Int J Thermal Sci 50(6):1001–1012

35. Rahimi M, Mehryar R (2012) Numerical study of axial heat conduction effects on the local Nusselt number at the entrance and ending regions of a circular microchannels. Int J Thermal Sci 59:87–94

36. Rosa P, Karayiannis TG, Collins MW (2009) Single phase heat transferrin microchannels: the importance of scaling effects. App Thermal Eng 29(17–18):3447–3468

37. Hung CY, Wu CM, Chen YN, Liou TM (2014) The experimental investigation of axial heat conduction effect on the heat transfer analysis in microchannel flow. Int J Heat Mass Transf 70:169–173

38. Ramiar A, Ranjbar AA, Hosseinizadeh SF (2012) Effect of axial conduction and variable properties on two dimensional conjugate heat transfer of Al_2O_3-EG/water mixture nanofluid in microchannel. J App Fluid Mech 5(3):79–87

39. Aghaei A, Khorasanizadeh H, Sheikhzadeh G, Abbaszadeh M (2016) Numerical study of magnetic field on mixed convection and entropy generation of nanofluid in a trapezoidal enclosure. J Magn Magn Mater 403:133–145

40. Pak BC, Cho Y (1998) Hydrodynamic and heat transfer study of dispersed fluids with submicron metallic oxide particle. Exp Heat Transf 11:151–170

41. Xuan Y, Roetzel W (2000) Conceptions for heat transfer correlation of nanofluids. Int J Heat Mass Transf 43:3701–3707

42. Duangthongsuk W, Wongwises S (2009) Measurement of temperature- dependent thermal conductivity and viscosity of the TiO_2-water nanofluid. Exp Thermal Fluid Sci 33:706–714

43. He Y, Jin Y, Chen H, Ding Y, Cang D, Lu H (2007) Heat transfer and flow behavior of aqueous suspensions of TiO_2 nanoparticles (nanofluids) flowing upward through a vertical pipe. Int J Heat Mass Transf 50:2272–2281

44. Said Z, Sabiha MA, Saidur R, Hepbasli A, Rahim NA, Mekhilef S, Ward TS (2015) Performance enhancement of a flat plate solar collector using titanium dioxide nanofluid and polyethylene glycol dispersant. J Clean Prod 92:343–353

45. Hamilton RL, Crosser OK (1962) Thermal conductivity of heterogeneous two-component systems. Ind Eng Chem Res 125:187–191

46. Einstein A (1906) A new determination of molecular dimension. Ann Phys 4:37–62

47. Brickman HC (1952) The viscosity of concentrated suspensions and solutions. J Chem Phys 20:571–581

48. Batchelor G (1977) The effect of Brownian motion on the bulk stress in the suspension of spherical particles. J Fluid Mech 83:97–117

49. Maxwell JCA (1881) A treatise on electricity and magnetism. Clarendon Press, Oxford

50. Shah RK (1975) Thermal entry length solutions for the circular tube and parallel plates. In: 3rd National Heat Mass Transfer Conference. IIT Bombay 1:11–75

51. Singh PK, Anoop KP, Sundararajan T, Das SK (2010) Entropy generation due to flow and heat transfer in nanofluids. Int J Heat Mass Transf 53:4757–4767

52. Ebrahimi A, Rikhtegar F, Sabaghan A, Roohi E (2016) Heat transfer and entropy generation in a microchannels with longitudinal vortex generators using nanofluids. Energy 101:190–201

53. Bazdidi-Tehrani F, Vasefi SI, Anvari AM (2019) Analysis of particle dispersion and entropy generation in turbulent mixed convection of CuO-water nanofluid. Heat Transf Eng 40(1–2):81–94

54. Bazdidi-Tehrani F, Sedaghatnejad M, Vasefi SI, Jolandan NE (2016) Investigation of mixed convection and particle dispersion of nanofluids in a vertical duct. Proc Inst Mech Eng C J Mech Eng Sci 230(20):3691–3705

55. Coleman HW, Steele WG (2009) Experimentation, validation and uncertainty analysis for engineers, 3rd edn. Wiley, Hoboken